



1 **Particle number concentrations and size distributions in the stratosphere: Implications of**  
2 **nucleation mechanisms and particle microphysics**

3 Fangqun Yu<sup>1</sup>, Gan Luo<sup>1</sup>, Arshad Arjunan Nair<sup>1</sup>, Sebastian Eastham<sup>2,3</sup>, Christina J. Williamson<sup>4</sup>,  
4 <sup>5, a</sup>, Agnieszka Kupc<sup>5,6</sup>, and Charles A. Brock<sup>5</sup>

5 <sup>1</sup> Atmospheric Sciences Research Center, University at Albany, Albany, New York, US

6 <sup>2</sup> Laboratory for Aviation and the Environment, Department of Aeronautics and Astronautics,  
7 Massachusetts Institute of Technology, Cambridge, MA 02139, USA

8 <sup>3</sup> Joint Program on the Science and Policy of Global Change, Massachusetts Institute of  
9 Technology, Cambridge, MA 02139, USA

10 <sup>4</sup> Cooperative Institute for Research in Environmental Sciences, University of Colorado,  
11 Boulder, CO 80309, USA

12 <sup>5</sup> Chemical Sciences Laboratory, National Oceanic and Atmospheric Administration, Boulder,  
13 CO 80305, USA

14 <sup>6</sup> Faculty of Physics, Aerosol Physics and Environmental Physics, University of Vienna, 1090  
15 Vienna, Austria

16 <sup>a</sup> now at: Climate Research Programme, Finnish Meteorological Institute, 00101 Helsinki,  
17 Finland and Institute for Atmospheric and Earth System Research/Physics, Faculty of Science,  
18 University of Helsinki, 00014 Helsinki, Finland.

19

20 Correspondence to: F. Yu ([fyu@albany.edu](mailto:fyu@albany.edu))

21

22 **Abstract.** While formation and growth of particles in the troposphere have been extensively  
23 studied in the past two decades, very limited efforts have been devoted to understanding these in  
24 the stratosphere. Here we use both Cosmics Leaving OUTdoor Droplets (CLOUD) laboratory  
25 measurements taken under very low temperatures (205–223K) and Atmospheric Tomography  
26 Mission (ATom) in-situ observations of particle number size distributions (PNSD) down to 3 nm  
27 to constrain nucleation mechanisms and to evaluate model simulated particle size distributions in  
28 the lowermost stratosphere (LMS). We show that the binary homogenous nucleation (BHN)  
29 scheme used in most of the existing stratospheric aerosol injection (a proposed method of solar  
30 radiation modification) modeling studies overpredict the nucleation rates by 3–4 orders of



31 magnitude (when compared to CLOUD data) and particle number concentrations in the  
32 background LMS by a factor  $\sim 2\text{--}4$  (when compared to ATom data). Based on a recently developed  
33 kinetic nucleation model, which gives rates of both ion-mediated nucleation (IMN) and BHN at  
34 low temperatures in good agreement with CLOUD measurements, both BHN and IMN occur in  
35 the stratosphere. However, IMN rates are generally more than one order of magnitude higher than  
36 BHN rates and thus dominate nucleation in the background stratosphere. In the Southern  
37 Hemisphere (SH) LMS with minimum influence of anthropogenic emissions, our analysis shows  
38 that ATom measured PNSDs generally have four apparent modes. The model captures reasonably  
39 well the two modes (Aitken mode and the first accumulation mode) with the highest number  
40 concentrations and the size-dependent standard deviations. However, the model misses an apparent  
41 second accumulation mode peaking around 300–400 nm, which is in the size range important for  
42 aerosol direct radiative forcing. The bi-mode structure of accumulation mode particles has also  
43 been observed in the stratosphere well above tropopause and in the volcano-perturbed stratosphere.  
44 We suggest that this bi-mode structure may be caused by the effect of charges on coagulation and  
45 growth, which is not yet considered in any existing models and may be important in the  
46 stratosphere due to high ionization rates and long lifetime of aerosols. Considering the importance  
47 of accurate PNSDs for projecting realistic radiation forcing response to stratospheric aerosol  
48 injection (SAI), it is essential to understand and incorporate such potentially important processes  
49 in SAI model simulations.

50

51

52



## 53 1. Introduction

54 Solar radiation modification (also known as solar geoengineering) approaches are being  
55 developed in response to the climate crisis (IPCC, 2021). They would temporarily offset climate  
56 change by reducing incoming sunlight, augmenting (currently inadequate) mitigation efforts and  
57 buying time to reduce atmospheric levels of CO<sub>2</sub>, which is the root cause of the climate crisis. A  
58 recent report by the National Academies of Sciences, Engineering and Medicine (NASEM)  
59 emphasizes the urgent need to have a comprehensive understanding of the feasibility and potential  
60 risks/benefits of solar climate intervention approaches (NASEM, 2021). Stratospheric aerosol  
61 injection (SAI) has demonstrated the most promise as proximately engineerable (Shepherd et al.,  
62 2009; Lockley et al., 2020; IPCC, 2021) and has been extensively studied using models (e.g.,  
63 GeoMIP: Kravitz et al., 2011; GLENS: Mills et al., 2017; Richter et al., 2022). The NASEM report  
64 (NASEM, 2021) pointed out that “the overall magnitude and spatial distribution of the forcing  
65 produced by SAI depends strongly on the aerosol size distribution” and “One of the research  
66 priorities for SAI is thus to address critical gaps in knowledge about the evolution of the aerosol  
67 particle size distribution”. In the stratosphere, sulfate aerosols are formed by nucleation, followed  
68 by condensational growth and coagulation, and lost by evaporation in the upper stratosphere and  
69 downward sedimentation into the troposphere (Turco et al., 1982). New particle formation (NPF)  
70 (or nucleation) affects not only the number abundance but also the size distributions of  
71 stratospheric particles (e.g., Brock et al., 1995; Lee et al., 2003). There is increasing evidence  
72 (Weisenstein et al., 2022, Laakso et al., 2022) that a careful treatment of microphysical processes  
73 is necessary for projecting realistic radiative forcing response to SAI.

74 The process of NPF under tropospheric conditions has been extensively explored over the last  
75 two decades through laboratory and field measurements, theoretical studies, and numerical  
76 simulations (e.g., Yu and Turco, 2000; Vehkamäki et al., 2002; Kulmala et al., 2004; Kirkby et al.,  
77 2011; Dawson et al., 2012; Zhang et al., 2012; Kürten et al., 2016; Yu et al., 2018; Kerminen et  
78 al., 2018; Lee et al., 2019). Although some of the advances in our understanding of nucleation  
79 gained in the last two decades can be applied to stratospheric conditions, focused studies  
80 specifically examining the mechanisms of NPF under stratospheric conditions are quite limited.  
81 Indeed, the H<sub>2</sub>SO<sub>4</sub>–H<sub>2</sub>O binary homogenous nucleation (BHN) parameterization developed two  
82 decades ago by Vehkamäki et al. (2002) (named BHN\_V2002 thereafter) has been used in most  
83 of SAI modeling studies when nucleation mechanism is considered (e.g., Weisenstein et al., 2022,  
84 Laakso et al., 2022). To our knowledge, the performance of this widely used BHN\_V2002 under  
85 stratospheric conditions has not been carefully examined, probably due to the lack of suitable  
86 in situ measurements of freshly nucleated particles in the stratosphere for constraining the scheme.  
87 In this regard, particle size distributions down to 3 nm measured in-situ during the NASA  
88 Atmospheric Tomography Mission (ATom) in the lowermost stratosphere (LMS) of both SH and  
89 NH in four different seasons (Williamson et al., 2019, 2021; Kupc et al., 2020; Brock et al., 2021)  
90 provide much-needed data to constrain our understanding of the nucleation and particle  
91 microphysics in the stratosphere. In addition, well-controlled CLOUD experiments taken under  
92 low temperature (within the range of stratosphere) can also be used to assess the performance of  
93 nucleation schemes under stratospheric conditions. Another important issue related to  
94 stratospheric particles is the role of ionization in nucleation. It is well established that nucleation  
95 of H<sub>2</sub>SO<sub>4</sub>–H<sub>2</sub>O on ions is favored over homogenous nucleation (Hamill et al., 1982; Yu and Turco,  
96 2000; Lovejoy et al., 2004; Kirkby et al. 2011; Yu et al., 2018) but the role of ionization in NPF



97 in the stratosphere has not been considered in any previous SAI studies (to our knowledge) in spite  
98 of the very high ionization rates in the stratosphere.

99 In this study, we use both CLOUD laboratory measurements taken under very low  
100 stratospheric temperatures and ATom PNSD measurements in LMS to constrain nucleation  
101 mechanisms and model simulated particle size distributions. For 3-D simulation of size-resolved  
102 stratospheric aerosols, we use the GEOS-Chem with the unified tropospheric-stratospheric  
103 chemistry-transport model with the size-resolved advanced particle microphysics (APM) package.  
104

## 105 **2. Model and data**

### 106 **2.1 GEOS-Chem/APM**

107 The GEOS-Chem model is a global 3-D model of atmospheric composition (e.g., Bey et al.,  
108 2001) and is continuously being improved (e.g., Luo et al., 2020; Holmes et al., 2019; Keller et al.,  
109 2014; Murray et al., 2012; Pye and Seinfeld, 2010; van Donkelaar et al., 2008; Evans and Jacob,  
110 2005; Martin et al., 2003). The GEOS-Chem tropospheric–stratospheric unified chemistry  
111 extension (UCX; Eastham et al., 2014), now the standard GEOS-Chem configuration, implements  
112 stratospheric chemistry, calculation of J-values for shorter wavelengths, and improved modeling  
113 of high-altitude aerosols. Extension of the chemistry mechanism to include reactions relevant to  
114 the stratosphere enables the capturing of stratospheric responses and troposphere–stratosphere  
115 coupling. UCX adds 28 species and 104 kinetic reactions, including 8 heterogeneous reactions,  
116 along with 34 photolytic decompositions. Atomic oxygen [both O(<sup>3</sup>P) and O(<sup>1</sup>D)] is explicitly  
117 modeled; although also of short lifetime in the stratosphere, these species are important in correctly  
118 modeling stratospheric chemistry. Photochemistry is extended up to the stratopause to high-energy  
119 photons (177 nm) using the Fast-JX model, which includes cross-section data for many species  
120 relevant to the troposphere and stratosphere. Photolysis rates respond to changes in the  
121 stratospheric ozone layer. Additional heterogeneous reactions (Kirner et al., 2011, Rotman et al.,  
122 2001, Shi et al., 2001) are included to capture seasonal ozone depletion. H<sub>2</sub>O is treated as a  
123 chemically-active advected tracer within the stratosphere. These permit chemical feedbacks  
124 between stratospheric ozone and aerosols and tropospheric photochemistry. The improved GEOS-  
125 Chem with coupled stratospheric–tropospheric responses has been evaluated with sonde and  
126 satellite measurements of O<sub>3</sub>, HNO<sub>3</sub>, H<sub>2</sub>O, HCl, ClO, NO<sub>2</sub> and stratospheric intrusions (Eastham  
127 et al., 2014; Gronoff et al., 2021; Knowland et al., 2022). Yu and Luo (2009) incorporated a size-  
128 resolved (sectional) APM package into GEOS-Chem, henceforth referred to as GC-APM. The  
129 APM separates secondary particles from primary particles, uses 40 bins to represent secondary  
130 particles with high size resolution for the size range important for the growth of nucleated particles  
131 to accumulation mode sizes, and contains options to calculate nucleation rates based on different  
132 nucleation schemes. APM is fully coupled with GEOS-Chem in both the troposphere and  
133 stratosphere, and is employed for the present study.

134 In the present study we have carried out GEOS-Chem-UCX/APM global simulations from  
135 01/2015 to 05/2018, with the first 17 months as spin-up and the remaining period covering ATom  
136 1-4 periods (06/2016–05/2018). The horizontal resolution is 4°×5° and there are 72 vertical layers.  
137 Emissions from different sources, regions, and species are computed via the Harvard-NASA  
138 Emissions Component (HEMCO) on a user-defined grid (Keller et al., 2014). Historical global  
139 anthropogenic emissions are based on the Community Emissions Data System (CEDS) inventory



140 (Hoesly et al., 2018). Regional anthropogenic emissions over the United States, Canada, Europe,  
141 and East Asia are replaced by regional emission inventories of the National Emissions Inventory  
142 (NEI, [https://www.epa.gov/air-emissions-inventories/2017-national-emissions-inventory-nei-](https://www.epa.gov/air-emissions-inventories/2017-national-emissions-inventory-nei-data)  
143 [data](https://www.epa.gov/air-emissions-inventories/2017-national-emissions-inventory-nei-data)), the Air Pollutant Emission Inventory (APEI, [https://www.canada.ca/en/environment-](https://www.canada.ca/en/environment-climate-change/services/pollutants/air-emissions-inventory-overview.html)  
144 [climate-change/services/pollutants/air-emissions-inventory-overview.html](https://www.canada.ca/en/environment-climate-change/services/pollutants/air-emissions-inventory-overview.html)), the Co-operative  
145 Programme for Monitoring and Evaluation of the Long-range Transmission of Air Pollutants in  
146 Europe (EMEP, <https://www.emep.int/index.html>), and the MIX Asian emission inventory (Li et  
147 al., 2017), respectively. Monthly mean aircraft emissions are generated based on the Aviation  
148 Emissions Inventory v2.0 (Stettler et al., 2011). The aircraft particle emissions include nucleation  
149 mode sulfate particles (Emission index =  $2 \times 10^{17}$  /kg-fuel, mean diameter = 9 nm, based on Kärcher  
150 et al., 2000), and black carbon and primary organic carbon (POC) particles. Global biomass  
151 burning is taken from Global Fire Emissions Database version 4 (van der Werf et al., 2017). The  
152 volcanic emissions of SO<sub>2</sub> are taken from AeroCom point-source data (Carn et al., 2015). Fixed  
153 global surface boundary conditions are applied for N<sub>2</sub>O, CFCs, HCFCs, halons, OCS and long-  
154 lived organic chlorine species (Eastham et al., 2014).

155

## 156 **2.2 Airborne ATom measurements of PNSD**

157 Measurements are essential in advancing our understanding of stratospheric aerosol properties  
158 and the fundamental processes governing these properties. NASA's Atmospheric Tomography  
159 Mission (ATom; Wofsy et al., 2021; Thompson et al., 2022) is a multi-agency effort that provides  
160 global in situ aircraft observations of the vertical structure of aerosols from near surface to ~12 km  
161 altitude. PNSDs are measured using the NOAA Aerosol Microphysical Properties (AMP) package  
162 (Brock et al., 2019) comprising nucleation-mode aerosol size spectrometer(s) (NMASS)  
163 (Williamson et al. 2018), ultra-high-sensitivity aerosol spectrometer(s) (UHSAS) (Kupc et al.  
164 2018), and a laser aerosol spectrometer (LAS) covering aerosol sizes from 3 nm to 4.5 μm. The  
165 aerosol number abundance can be obtained by integrating the PNSD measurements.

166

## 167 **2.3 The CLOUD (Cosmics Leaving Outdoor Droplets) measurements**

168 Laboratory measurements of nucleation rates as a function of key controlled parameters have  
169 been carried out in a 26.1 m<sup>3</sup> stainless steel cylinder chamber at the European Organization for  
170 Nuclear Research (CERN), in the framework of the CLOUD experiment (Cosmics Leaving  
171 Outdoor Droplets) (e.g., Kirkby et al., 2011; Kürten et al., 2016; Dunne et al., 2016). Some of  
172 these experiments were conducted at the temperature in the range of those in the stratosphere  
173 (Kirkby et al., 2011; Dunne et al., 2016) which are used in this study to evaluate nucleation  
174 schemes under stratospheric conditions.

175

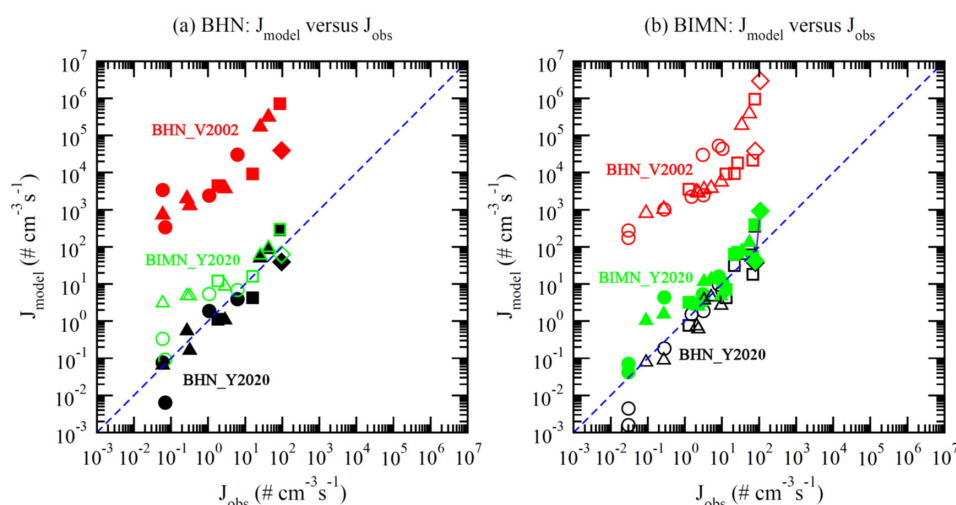
## 176 **3. Results**

### 177 **3.1 H<sub>2</sub>SO<sub>4</sub>-H<sub>2</sub>O binary homogeneous nucleation (BHN) and binary ion-mediated nucleation (BIMN) under stratospheric conditions**

178 Nucleation is one of the microphysical processes influencing particle size distributions in the  
179 stratosphere (Turco et al., 1982) The CLOUD measurements under a wide range of well-controlled  
180 conditions (Kirkby et al., 2011; Dunne et al., 2016) provide a unique set of data to evaluate the  
181 nucleation theories. Yu et al. (2020) compared nucleation rates calculated based on a number of  
182 commonly used aerosol nucleation parameterizations with the CLOUD measurements. Here we  
183



184 specifically examine the comparison under stratospheric conditions where temperature is below ~  
185 230 K. Since ammonia concentrations in the stratosphere are generally negligible, we focus on  
186 binary nucleation in the present study. The contribution of organics to particle formation, growth,  
187 and compositions in the upper troposphere and LMS has been investigated in several studies (Kupc  
188 et al., 2020; Murphy et al., 2021; Williamson et al., 2021). Because of the lack of information with  
189 regard to the low volatile gaseous organic species, the possible role of organics in new particle  
190 formation in LWS is not considered in the present study.  
191



192  
193 **Figure 1.** Comparison of nucleation rates based on three different schemes with CLOUD  
194 measurements within the low temperature range ( $T = 205\text{--}223\text{ K}$ ) as that in the stratosphere for (a)  
195 binary homogeneous nucleation (no ionization) and (b) ion nucleation (at the presence of  
196 ionization rates  $2.51 - 110\text{ ion-pairs cm}^{-3}\text{s}^{-1}$ ). The different nucleation schemes shown are: BHN  
197 of Vehkamäki et al. (2002) (BHN\_V2002), BHN of Yu et al. (2020) (BHN\_Y2020), and BIMN  
198 of Yu et al. (2020) (BIMN\_Y2020). For comparison, under binary condition of (a), BIMN rates at  
199  $Q = 20\text{ ion-pairs cm}^{-3}\text{s}^{-1}$  are given while under binary ion nucleation condition of (b), BHN rates  
200 are also given.  $[\text{H}_2\text{SO}_4]$  values range from  $10^6$  to  $3 \times 10^7\text{ cm}^{-3}$  and are separated into four groups  
201 in the plots (Circles:  $10^6 - 5 \times 10^6\text{ cm}^{-3}$ ; triangles:  $5 \times 10^6 - 10^7\text{ cm}^{-3}$ ; Squares:  $10^7 - 1.5 \times 10^7\text{ cm}^{-3}$ ;  
202 Diamonds:  $1.5 \times 10^7 - 3 \times 10^7\text{ cm}^{-3}$ ).

203  
204 Figure 1 compares BHN and BIMN rates based on three different schemes with CLOUD  
205 measurements under stratospheric temperature range ( $T = 205\text{--}223\text{ K}$ ). The nucleation schemes  
206 shown are: BHN of Vehkamäki et al. (2002) (BHN\_V2002), BHN of Yu et al. (2020)  
207 (BHN\_Y2020), and BIMN of Yu et al. (2020) (BIMN\_Y2020). To show the relative importance  
208 of homogeneous versus ion nucleation, BIMN rates at  $Q = 20\text{ ion-pairs cm}^{-3}\text{s}^{-1}$  were given under  
209 binary homogeneous condition in Fig. 1a and BHN rates were also given under binary ion  
210 nucleation condition in Fig. 1b. Nucleation rates based on BHN\_V2002 are consistently 3–5 orders  
211 of magnitude higher than those observed under  $\text{H}_2\text{SO}_4\text{--H}_2\text{O}$  binary nucleation conditions without  
212 (Fig. 1a) and with (Fig. 1b) the effect of ionizations, while those based on BHN\_Y2020 and  
213 BIMN\_Y2020 are close to the observed values. It should be noted that similar to the CLOUD

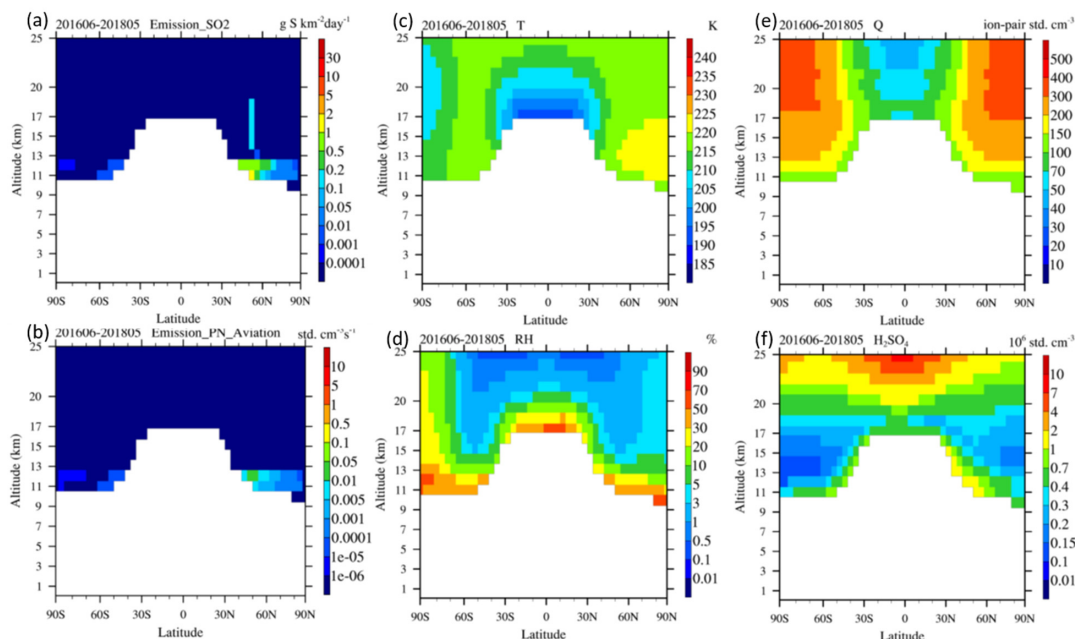




214 measurements with the effect of ionization, BHN rates are included in the BIMN rates (Yu et al.,  
215 2018) and the difference between BIMN and BHN rates indicates the contribution of ion mediated  
216 or induced nucleation. Under the conditions of Fig. 1a, assuming ionization rate of 20 ion-pairs  
217  $\text{cm}^{-3}\text{s}^{-1}$  (within the range of its typical value in the stratosphere) the BIMN rates are about one  
218 order of magnitude higher than BHN rates when the nucleation rates are below  $\sim 5 \text{ cm}^{-3}\text{s}^{-1}$  but  
219 close to BHN rates when nucleation rates are above  $\sim 5 \text{ cm}^{-3}\text{s}^{-1}$ . Similar difference between  
220 BHN\_Y2020 and BIMN\_Y2020 can also be seen in Fig. 1b, indicating the importance of ion  
221 nucleation at relatively lower nucleation rates (mostly associated with relatively lower  $[\text{H}_2\text{SO}_4]$ )  
222 and dominance of homogeneous nucleation at higher nucleation rates (associated with larger  
223  $[\text{H}_2\text{SO}_4]$ ). As we show next,  $[\text{H}_2\text{SO}_4]$  in the background stratosphere is generally quite low and  
224 thus ion nucleation dominates but BHN can become important in the  $\text{SO}_2$  plumes injected into the  
225 stratosphere.  
226

### 227 3.2 Nucleation rates and particle number concentrations in the stratosphere

228 Figure 2 shows the zonal mean  $\text{SO}_2$  emission ( $\text{SO}_2_{\text{emit}}$ ), particle number emitted by aviation  
229 ( $\text{PN}_{\text{aviation}}$ ), temperature ( $T$ ), relative humidity (RH), ionization rate ( $Q$ ), and  $[\text{H}_2\text{SO}_4]$  averaged  
230 during the two-year period (06/2016–05/2018) covering ATom 1–4. To focus on lower stratosphere  
231 (LS), only the values of these variables in the stratosphere (grid boxes with more than 50% time  
232 above tropopause) are shown. The  $\text{SO}_2$  emissions include all sources including volcanos and  
233 aviation. During this period, there was one relatively strong volcanic event that injected  $\text{SO}_2$  into  
234 an altitude of  $\sim 14\text{--}18 \text{ km}$  at  $52^\circ\text{N}$  (Fig. 2a). Aviation emission is generally limited to below  $\sim 12.5$   
235  $\text{km}$  altitude. Based on MERRA2 meteorology data, which is used to drive GEOS-Chem, almost  
236 all of grid boxes at  $12 \text{ km}$  are under the tropopause in the tropics ( $30^\circ\text{N}\text{--}30^\circ\text{S}$ ), most of grid boxes  
237 at  $12 \text{ km}$  in the high latitude regions ( $60^\circ\text{N}\text{--}90^\circ\text{N}$ ,  $60^\circ\text{S}\text{--}90^\circ\text{S}$ ) are above tropopause, and some  
238 fractions of grid boxes at  $12 \text{ km}$  in the middle latitude regions ( $30^\circ\text{N}\text{--}60^\circ\text{N}$ ,  $30^\circ\text{S}\text{--}60^\circ\text{S}$ ) are above  
239 tropopause. As can be seen from Fig. 2b, some of aviation emissions in the middle and high latitude  
240 regions are in the LMS, and the amount emitted into NH LMS is much higher (by several orders  
241 of magnitude) than that in SH. The temperature in the LS ranges from  $190\text{--}225\text{K}$ , with the lowest  
242 value in the region just above tropical tropopause (Fig. 2c). RH in LS has highest values near  
243 tropopause but drops quickly with increasing altitude, from  $\sim 30\text{--}50\%$  near tropopause to  $\sim 0.1\text{--}1\%$   
244 at  $\sim 25 \text{ km}$  in the tropical and middle latitudes (Fig. 2d). The spatial variations of  $T$  and RH have  
245 important effects on nucleation in LS. The cosmic ray induced ionization rate in LS has large  
246 latitudinal gradient, ranging from  $\sim 40\text{--}100 \text{ ion-pair std. cm}^{-3}\text{s}^{-1}$  in the tropics to  $100\text{--}400 \text{ ion-pair}$   
247  $\text{std. cm}^{-3}\text{s}^{-1}$  in middle and high latitude region (Fig. 2e). The high ionization rates may have  
248 important implication for particle microphysics in LS, which will also be discussed in Section 3.3.  
249  $\text{H}_2\text{SO}_4$  is the most important aerosol precursor in LS and its concentration depends on  $\text{SO}_2$   
250 concentrations and oxidation, condensation sink, and its vapor pressure that depends on  $T$  and RH.  
251 The annual mean  $[\text{H}_2\text{SO}_4]$  (Fig. 2f) has large spatial variations, ranging from a minimum of  $\sim 1\text{--}2$   
252  $\times 10^5 \text{ std. cm}^{-3}$  at altitudes of  $\sim 12\text{--}15 \text{ km}$  in polar regions to  $\sim 4\text{--}20 \times 10^5 \text{ std. cm}^{-3}$  close to the  
253 tropopause. From  $\sim 18\text{--}25 \text{ km}$  (well above the ATom measurement altitude),  $[\text{H}_2\text{SO}_4]$  increases  
254 with altitude, mainly due to the increasing  $\text{H}_2\text{SO}_4$  vapor pressure associated with vertical changes  
255 of  $T$  (Fig. 2c) and RH (Fig. 2d).  
256  
257



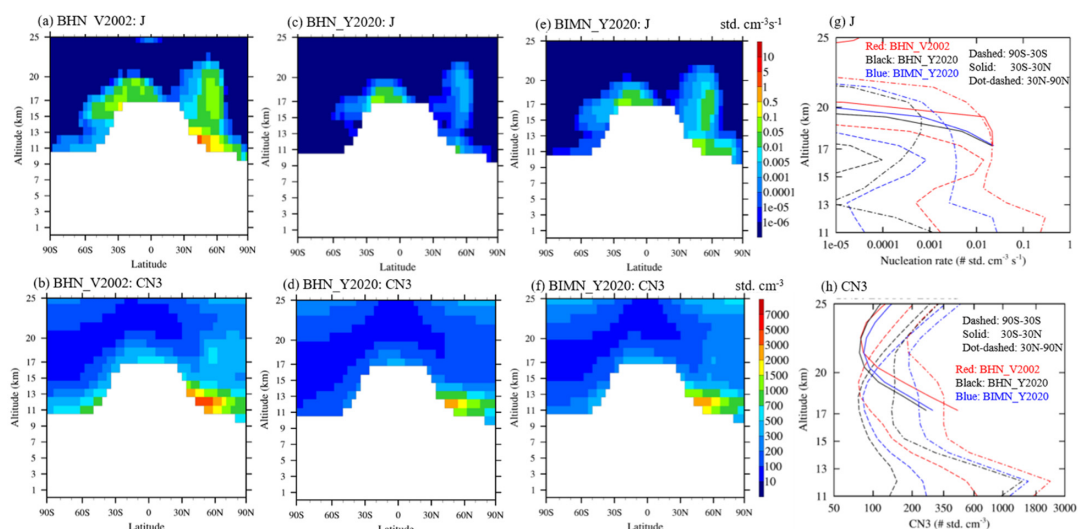
258  
259 **Figure 2.** Zonal mean  $\text{SO}_2$  emit, PN Emit,  $T$ , RH,  $Q$ , and  $[\text{H}_2\text{SO}_4]$  averaged during the two-year  
260 period (06/2016-05/2018) covering ATom 1-4. To focus on the lower stratosphere, only the values  
261 of these variables in grid boxes with more than 50% time above tropopause and below 25 km are  
262 shown.

263  
264 To demonstrate the effect of nucleation schemes on simulated aerosol properties, we compare  
265 in Fig. 3 zonal mean and vertical profiles of nucleation rates (J) and number concentrations of  
266 condensation nuclei larger than 3 nm (CN3) simulated based on the three nucleation schemes:  
267 BHN\_V2002, BHN\_Y2020, and BIMN\_Y2020. In all three schemes, the aviation emissions of  
268 both  $\text{SO}_2$  (Fig. 2a) and particle numbers (Fig. 2b) are the same. The model simulations indicate  
269 that NPF occurs in the lower stratosphere but is mostly confined to LMS except in the area of  
270 volcano injection (for example, above  $\sim 14$  km around  $\sim 52^\circ\text{N}$ ). There exist large differences  
271 in the nucleation rates predicted by the three schemes (noting the logarithmic color scale), with  
272 BHN\_V2002 rates generally 1–4 orders of magnitude higher while BIMN\_Y2020 rates  $\sim$  one  
273 order of magnitude higher than those based on BHN-Y2020. The difference between  
274 BIMN\_Y2020 and BHN\_V2002 rates are smaller in the LMS over tropics ( $0^\circ\text{S}$ - $30^\circ\text{S}$ ) where  
275 temperature is the lowest (see Fig. 2c). The magnitudes of differences are consistent with  
276 comparisons with CLOUD measurements (Fig. 1). The difference in nucleation rates leads to  
277 substantial difference in CN3 in LMS, with those based on BHN\_V2002 a factor 2–5 higher than  
278 those based on BHN\_Y2020 in LMS. LMS CN3 based on BIMN\_Y2020 is about 50% higher than  
279 that of BHN\_Y2020. Compared to the difference in nucleation rates, the differences in CN3 is  
280 much smaller. This is expected because on one hand only a small fraction of nucleated particles  
281 survive the coagulation scavenging and grow beyond 3 nm, and on the other hand direct emission  
282 of particle numbers from aviation (Fig. 2b; treated as direct emission but most of these are actually





283 nucleated on chemi-ions in the exhaust plume shortly after emission) (Brock et al., 2000) and  
284 transport provide substantial amount of CN3 even without nucleation. Nevertheless, nucleation is  
285 still significant enough to affect the CN3. It is interesting to note that CN3 based on BIMN\_Y2020  
286 is higher at altitudes  $> \sim 22$  km (Fig. 3h), which is associated with higher nucleation rates based  
287 on BIMN\_Y2020 than those based on BHN\_V2002 and BHN\_Y2020 within the altitude range of  
288 35–55 km. It can be seen from Fig. 3 that the simulations based on three nucleation schemes all  
289 show large hemispheric difference in particle number concentrations (by a factor of  $\sim 3$ –6) in LMS  
290 at middle and high latitudes, consistent with the ATom measurements (Williamson et al., 2021).  
291 Our sensitivity study (by turning off aviation emission, not shown, to be reported in a separate  
292 study) indicates this large hemispheric difference is largely caused by aviation emissions,  
293 confirming the analysis of Williamson et al. (2021).  
294

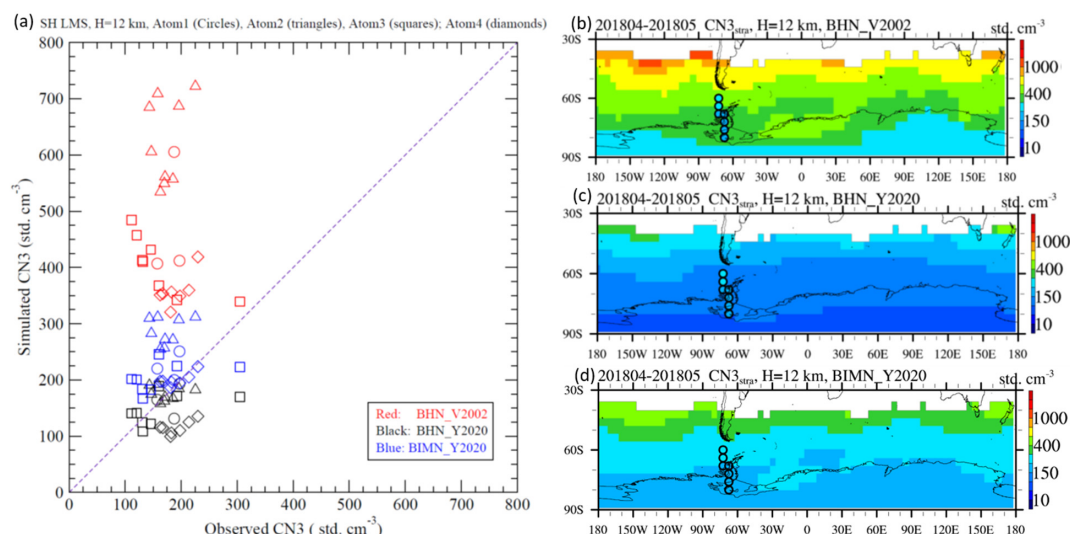


295  
296 **Figure 3.** Model simulated zonal mean and vertical profiles of nucleation rates ( $J$ ; upper panels)  
297 and number concentrations of particles larger than 3 nm (CN3; lower panels) in the stratosphere  
298 during the two-year period covering ATom 1–4 (06/2016– 05/2018), based on three nucleation  
299 schemes (a&b: BHN\_V2002, c&d: BHN\_Y2020, and e&f: BIMN\_Y2020). The vertical profiles  
300 in (g) and (h) are averaged for three latitude zones (90S–30S, 30S–30N, and 30N–90N). The values  
301 for those grids with at least 50% of time above the tropopause are shown.

302  
303 While it is difficult to observe nucleation rates in the stratosphere, the measurement of freshly  
304 nucleated nanoparticles can be used to constrain nucleation schemes. Figure 4a compares the  
305 model simulated CN3 (all particles with diameter larger than 3 nm, with the upper size limit of 12  
306  $\mu\text{m}$  corresponding to the size of last model bin) based on the three nucleation schemes at altitudes  
307 of around 12 km in SH middle and high altitudes during four seasons with the corresponding ATom  
308 1–4 observations. As an example, Figures 4b–d show the model simulated horizontal distributions  
309 of CN3 at 12 km altitude during ATom 4 with the values and locations of ATom4 CN3 data  
310 overlaid. We choose SH for comparison, as it represents the background stratosphere with



311 minimum influence of anthropogenic emissions (i.e., aviation) (Fig. 2b), to avoid the uncertainty  
312 associated with aviation emissions. In Figure 4, the model results are two-month average  
313 corresponding to the flight months of each ATom campaign while the measurement data points  
314 shown are those sampled within the altitudes range of 11.5–12.5 km, in the stratosphere  
315 (ozone>250 ppbv and RH<10%, following the same stratosphere definitions as in Murphy et al.  
316 (2021) and Williamson et al. (2021)), and averaged to a 4°x5° gridbox for comparison with  
317 modeled results. The impact of nucleation scheme on CN3 can be clearly seen: BHN\_V2002  
318 overpredicted CN3 by a factor of 2–4, BHN\_Y2020 slightly underpredicted CN3, and  
319 BIMN\_Y2020 slightly overpredicted CN3. The larger vertical spread in CN3 from BHN\_V2002  
320 is caused by the large CN3 latitude gradient associated with higher nucleation near tropopause  
321 (Fig. 3). The comparisons above show that the ATom measurements provide a good constraint on  
322 our understanding of the processes controlling CN3 in the LMS at mid-high latitudes.  
323



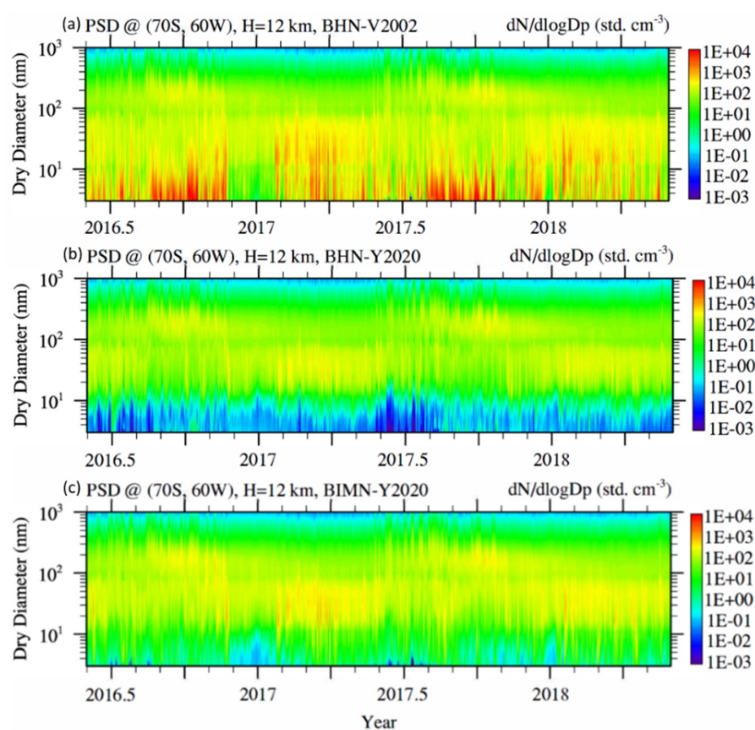
324  
325 **Figure 4.** CN3 at altitudes of around 12 km in SH middle and high latitudes: (a) Model simulated  
326 versus observed during ATom 1-4 (Circles: ATom1; Triangles: ATom2; Squares: ATom3;  
327 Diamonds: ATom4); (b-d) model simulated horizontal distributions corresponding to ATom 4  
328 based on three different nucleation schemes (BHN\_V2002, BHN\_Y2020, and BIMN\_Y2020),  
329 with the values and locations of ATom 4 CN3 measurements shown in the circles.

330  
331 **3.3 PNSDs in the stratosphere**

332 Figure 5 shows the model simulated evolution of PNSDs at an altitude of 12 km over a site in  
333 SH (70°S, 60°W) during the two-year ATom period based on the three different nucleation  
334 schemes. The PNSDs shown in Fig. 5 are averaged into four different seasons corresponding to  
335 the months of ATom 1-4 field campaigns and are presented in Fig. 6 for comparison with the  
336 observed mean PNSDs in SH LMS (Williamsons et al., 2021). It should be noted that modeled  
337 PNSDs in Fig. 6 are two-month average at one fixed site at an altitude of 12 km (in the region  
338 where many of SH LMS measurements were taken, see Fig. 4) while the observed ones are



339 averaged over all SH LMS air mass sampled during the corresponding ATom campaign. While  
340 the comparison in Fig. 6 is not exactly coterminous, it allows us to make quantitative comparisons  
341 of modeled and observed PNSDs. To take into account the variations in both model and observed  
342 PNSDs, standard deviations are shown as error bars in the measured and modeled curves based on  
343 BIMN\_Y2020.  
344

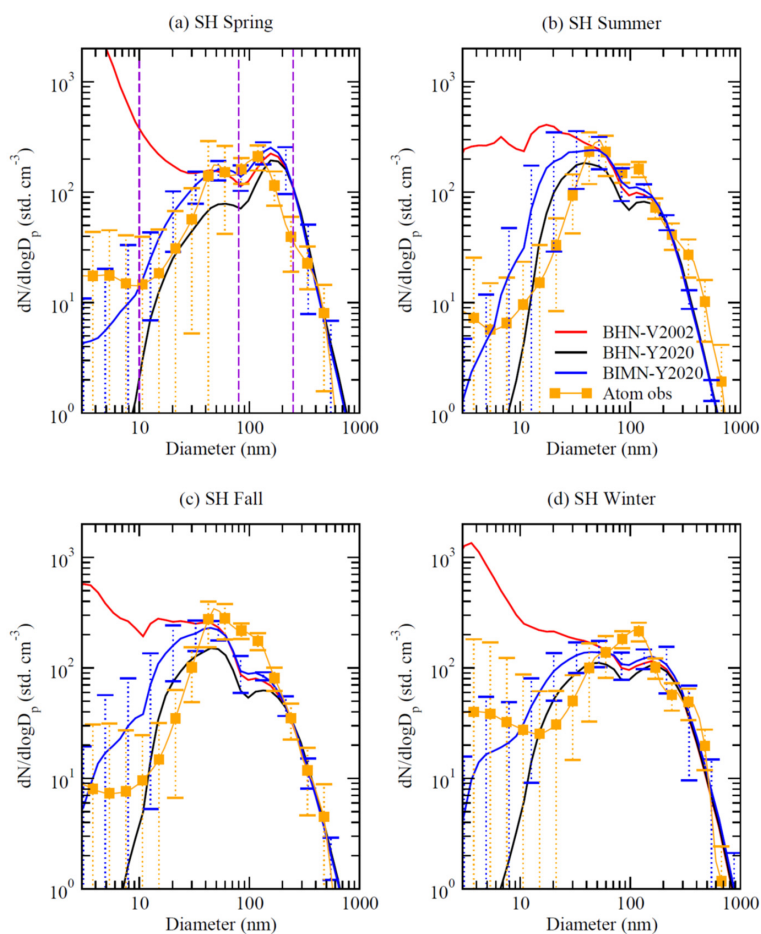


345  
346 **Figure 5.** Model simulated evolution of PSDs at a site in SH (70S, 60 W) at altitude of 12 km  
347 based on three nucleation schemes (BHN\_2002, BHN\_Y2020, and BIMN\_Y2020).

348  
349 Figures 5 and 6 show that PNSDs in the background LMS have multiple modes: a nucleation  
350 mode (NuclM:  $\lesssim 10$  nm), an Aitken mode (AitkenM:  $\sim 10 - 80$  nm), and two accumulation modes  
351 (AccuM1:  $\sim 80 - 250$  nm and AccuM2:  $\sim 250 - 700$  nm). It should be noted that these modes  
352 are not the same size limits as those presented in the public ATom dataset. The model based on all  
353 three nucleation schemes generally captures the AitkenM and AccuM1 and the existence of a  
354 minimum in PNSDs around 80 nm, although there exist differences. Interestingly, the relative  
355 height (or peak values of  $dN/d\log D_p$ ) of AitkenM and AccuM1 has strong seasonal variations. The  
356 model captures a relatively higher AitkenM in SH Summer and Fall and a higher AccuM1 in SH  
357 Spring. The model simulated PNSDs also agree well with the measurements in term of the size-  
358 dependent standard deviations: relatively smaller standard deviations for AccuM1 and larger size  
359 part of AitkenM and much larger standard deviations for NuclM, smaller size part of AitkenM,  
360 and AccuM2. While the larger standard deviations for NuclM is understandable because of NPF,



361 it is surprising for AccuM2. The AccuM2 particles have relatively long lifetime and are expected  
362 to be well-mixed (and thus have small variations) in LS. The transport of AccuM2 particles from  
363 UT may contribute to the larger variations. Murphy et al. (2021) showed the chemical signature  
364 of this transported mode, and here we show that the variation in the size distribution may also  
365 contain information about the mixing of UT particles into LMS. Compared to the observations,  
366 the model simulated AccuM2 standard deviations are larger in SH Winter and Spring but are  
367 smaller in SH Summer and Fall. The possible reasons for the large variations of AccuM2 in LMS  
368 and the differences between model simulations and measurements remain to be studied.



369  
370 **Figure 6.** Model simulated seasonal mean PSDs at a site in SH (70°S, 60°W) at altitude of 12 km  
371 based on three nucleation schemes and comparisons with the corresponding ATom measurements  
372 (a: SH Spring 09–10/2017, b: SH Summer 01–02/2017, c: SH Fall 04–05/2018, and d: SH Winter  
373 06–07/2016). To take into account the variations in both model and observed PNSDs, standard  
374 deviations are shown as error bars in the measured and modeled curves based on BIMN\_Y2020.  
375 Three vertical dashed lines at 10 nm, 80 nm, and 250 nm are drawn in (a) to guide the eye to the  
376 four modes discussed in the text.



377

378

379

380

381

382

383

384

385

386

387

388

389

390

391

392

393

394

395

396

397

398

399

400

401

402

403

404

405

406

407

408

409

410

411

412

413

414

415

416

417

418

419

The large impacts of nucleation schemes on PNSDs, especially those smaller than 100 nm, can be seen in Fig. 6. The formation rates and concentrations of nucleation mode particles are very high based on BHN\_V2002 (peak  $dN_{\log D_p}$  values reaching well above  $10^3 \text{ std. cm}^{-3}$ ), negligible based on BHN\_Y2020 ( $dN_{\log D_p}$  values for particles  $<10 \text{ nm}$  are generally below  $1 \text{ std. cm}^{-3}$ ), and moderate based on BIMN\_Y2020. When compared to the observed values, the number concentrations of particles within 3–10 nm based on BHN\_V2002 are 1–2 orders of magnitude too high but those based on BHN\_Y2020 are 1–2 orders of magnitudes too low, while those based on BIMN\_Y2020 are of the same order of magnitude. The impact of nucleation schemes on NuclM propagates into the AitkenM and AccuM1, with BHN\_Y2020 giving the lowest number concentrations while BHN\_V2002 gives the highest AitkenM and BIMN\_Y2020 gives the highest AccuM1. It is interesting to note that AccuM1 based on BIMN\_Y2020 is higher than that based on BHN\_V2002 although BHN\_V2002 predicts higher NuclM and AitkenM, indicating a non-linear interaction among nucleation, growth, and coagulation.

There exist a number of differences in the simulated and observed PNSDs. Firstly, measurements indicate a slight increase of  $dN_{\log D_p}$  with decreasing sizes for particles  $< 10 \text{ nm}$  but the simulated PNSDs based on BIMN\_Y2020, the scheme mostly consistent with CLOUD measurements and predicting NuclM concentrations closest to those observed, decreases with decreasing sizes for particles  $< 10 \text{ nm}$ . The possible reasons of the difference remain to be investigated but probably are associated with uncertainty in nucleation rates and size-dependent growth rates of freshly nucleated particles, and/or the fact that ATom observations are bias towards daytime. In addition, the small number of particles in this mode is likely within the uncertainty in the ATom measurements (about 7% of the total number of particles), so that this measured mode may not be significant. Secondly, the model appears to overpredict the smaller size part ( $\sim 10\text{--}40 \text{ nm}$ ) of AitkenM although it is close to the larger part of the mode ( $\sim 40\text{--}80 \text{ nm}$ ). The overprediction may be a result of the underestimated growth rates or coagulation scavenging rates of these particles or overpredicted growth rates of NuclM particles. Thirdly, the model generally overpredicts the mean mode sizes of AccuM1 and underpredicts the concentrations of the mode except in SH Spring. The nucleation schemes have observable effects on the concentrations and mean sizes of AccuM1 and overall the simulations based on BIMN\_Y2020 are in stronger agreement with measurements. Finally, the observed PNSDs show a clear AccuM2 in all seasons except Fall but the model does not predict the existence of the mode at all. AccuM2 particles are within the size range with most efficient scattering of solar radiation and thus are important for SAI. It is therefore necessary to identify the sources of this difference and to improve the model.

As pointed out earlier, the comparison in Fig. 6 does not exactly match in terms of time and location, which likely contributes to some of the differences shown in Fig. 6. Some of the differences can also be caused by the uncertainties in the model in term of emissions, transport, chemistry, aerosol microphysics, and deposition. Nevertheless, some of these differences, especially the shape of PNSDs (AccuM2, NuclM, etc.), are unlikely to be fully accounted for by the above-mentioned possible mismatch or model uncertainties and thus may indicate that some fundamental processes are not represented in the model. One possible cause of the differences is that the transport of organic-sulfate particles from UT (Murphy et al., 2014, 2021) is not properly



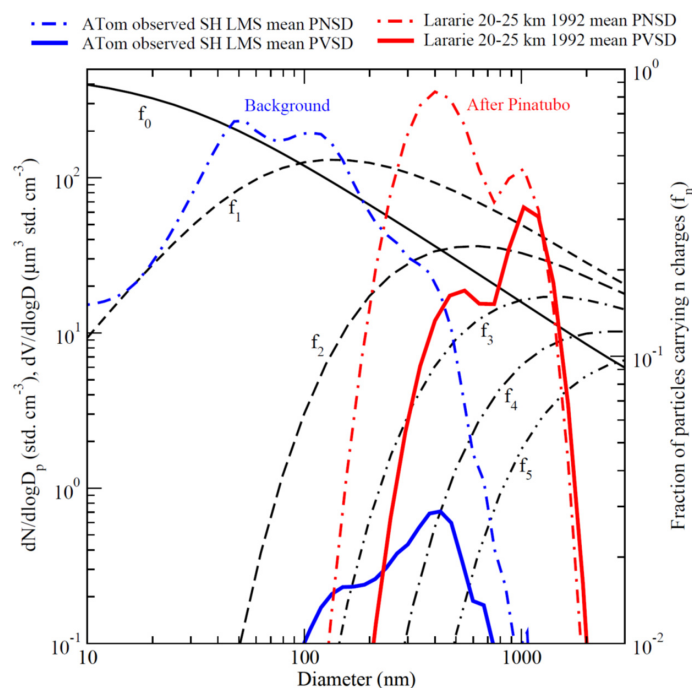


420 simulated by the model. Based on size-resolved particle composition measurements, Murphy et al.  
421 (2021) showed that the LMS accumulation mode particles (diameter  $\sim 0.1$  and  $1.0 \mu\text{m}$ ) have at  
422 least two modes: the larger mode consists mostly of sulfuric acid particles produced in the  
423 stratosphere, and the smaller mode consists mostly of organic-sulfate particles transported from  
424 the troposphere. Murphy et al. (2014) showed that the fraction of organic-sulfate aerosols above  
425 tropopause decreases quickly with altitudes. While the organic-sulfate mode aerosols from UT  
426 may contribute to the bi-mode structure of accumulation mode particles in the LMS observed  
427 during ATom, it is unlikely to contribute to the bi-mode structure of particles larger than  $\sim 200$  nm  
428 observed at altitude above  $\sim 20$  km both in the background and in volcano perturbed stratosphere  
429 (Deshler et al., 2013, 2019; also see Fig. 7). Here, we suggest that the role of charges on  
430 coagulation and growth of particles in the stratosphere could be another process causing the bi-  
431 mode of large particles in the stratosphere.

432 As shown Fig. 2e, ionization rates are high in LS, ranging from  $\sim 40$ – $100$  ion-pair  $\text{std. cm}^{-3}\text{s}^{-1}$ .  
433 Due to their low number concentrations ( $\sim 100$ – $1000$   $\text{std. cm}^{-3}$ ) but long lifetime, particles in the  
434 stratosphere are expected to be in charge equilibrium. Figure 7 shows mean particle number size  
435 distribution (PNSD) and particle volume size distribution (PVSD) observed during ATom 1-4 in  
436 SH LMS and measured within 20-25 km altitude over Larrie WY in 1992, and fraction of particles  
437 carrying  $n$  charges based on the modified Boltzmann equilibrium equation (Clement and Harrison,  
438 1992). The bi-mode structure of accumulation mode particles can be clearly seen in both  
439 background and volcano perturbed stratosphere. It should be noted that while the smaller mode  
440 generally dominates the number concentrations, the larger mode dominates mass concentrations.  
441 Under equilibrium more particles are charged (i.e.,  $1-f_0 > 50\%$ ) than neutral ( $f_0$ ) for particles with  
442 diameter larger than  $\sim 80$  nm and a significant fraction ( $> 25\%$ ) of particles larger than 300 nm  
443 carrying multiple charges. While the equilibrium charge fraction is small for NuclM particles ( $\lesssim$   
444 10 nm), this fraction can be much larger when nucleation on ions occurs, which is consistent with  
445 the observed overcharging of freshly nucleated particles (Laakso et al. 2007; Yu and Turco, 2008).  
446 Particle coagulation rates are influenced by forces exerted between colliding particles, including  
447 van der Waals and electrostatic forces, which can modify the effective collision cross section and  
448 sticking coefficient. The van der Waals force has been shown to be important in the stratosphere  
449 (English et al., 2011, 2012) and has been considered in the simulations shown above. The effects  
450 of charges on coagulation and implications for PNSDs in the stratosphere have not yet been studied  
451 (to our knowledge). Since coagulation is a dominant process for the growth of accumulation mode  
452 particles in the stratosphere, we hypothesize that differential coagulation rates for neutral and  
453 charged particles in accumulation modes can potentially act as a physical process separating the  
454 modeled single accumulation mode (Fig. 6) into two modes (AccuM1 and AccuM2) as observed.  
455 Further research is needed to test this hypothesis. In addition to affecting coagulation, charge on  
456 small particles can also enhance the growth rate due to ion-dipole interactions of condensing  
457 molecules with charged particles (Nadykto and Yu, 2005). This enhancement is expected to be  
458 stronger in the stratosphere because of lower temperature (Nadykto and Yu, 2005). Beside these,  
459 Svensmark et al. (2020) showed that the condensation of ion clusters can enhance particle growth  
460 rates. How much the enhanced coagulation and growth rates of charged particles may shape  
461 PNSDs and modes in the stratosphere remains to be investigated.

462





463  
 464 **Figure 7.** ATom 1-4 mean observed particle number size distribution (PNSD, or  $dN/d\log D_p$ ) and  
 465 particle volume size distribution (PVSD, or  $dV/d\log D_p$ ) in SH LMS, balloon-borne measured  
 466 mean PNSD and PVSD within 20-25 km altitude over Lararie WY in 1992, and fraction of  
 467 particles carrying  $n$  ( $n = 0, 1, 2, 3, 4,$  and  $5$ ) charges based on the modified Boltzmann equilibrium  
 468 equation (Clement and Harrison, 1992). Note that  $f_n$  with  $n \geq 1$  including both positive and negative  
 469 charges, i.e., for example, half of  $f_1$  carrying one negative charge while the other half positive.

470

#### 471 **4. Summary and Discussions**

472 Interest in stratospheric aerosols has been increasing in recent years, due to the ongoing  
 473 discussion about the plausibility, potential benefits and risks of offsetting climate change through  
 474 stratospheric aerosol injection (SAI) to buy time for reduction of  $\text{CO}_2$  in the atmosphere. Recent  
 475 studies indicate the dependence of SAI efficiency on the particle size distribution (NASEM, 2021)  
 476 and thus it is critical to improve foundational understanding and model representation of aerosol  
 477 microphysics processes controlling the evolution of stratospheric aerosols, both under background  
 478 conditions and perturbed scenarios. While formation and growth of particles in the troposphere  
 479 have been extensively studied in the past two decades, very limited efforts have been devoted to  
 480 understanding these in the stratosphere.

481 In the present study we use both CLOUD laboratory measurements taken under very low  
 482 stratospheric temperatures and ATom in-situ observations of particle number size distributions  
 483 (PNSD) down to 3 nm to constrain nucleation schemes and model-simulated particle size  
 484 distributions in the lowermost stratosphere (LMS). We show that the binary homogenous  
 485 nucleation scheme used in most of the existing SAI modeling studies overpredicts the nucleation  
 486 rates by 3–4 orders of magnitude (when compared to CLOUD data), leading to significant



487 overprediction of particle number concentrations in the background stratosphere (by a factor of 2–  
488 4 in SH LMS, compared to ATom data). Based on a recently developed kinetic nucleation model  
489 which provides rates of both ion-mediated nucleation (IMN) and BHN at low temperatures in good  
490 agreement with CLOUD measurements, both BHN and IMN occur in the stratosphere but IMN  
491 rates are generally more than one order of magnitude higher than BHN rates and thus dominate  
492 nucleation in the background stratosphere.

493 In the SH LMS that has minimal influences from anthropogenic emissions, our analysis shows  
494 that ATom-measured PNSDs generally have four apparent modes: a nucleation mode (NuclM:  $\lesssim$   
495 10 nm), which may not be statistically significant, an Aitken mode (AitkenM:  $\sim$ 10–80 nm), and  
496 two accumulation modes (AccuM1:  $\sim$  80–250 nm and AccuM2:  $\sim$  250–700 nm). The model  
497 generally captures the AitkenM and AccuM1 and the existence of a minimum in PNSDs at  $\sim$  80  
498 nm, although there are differences. The model captures a relatively higher AitkenM in SH Summer  
499 and Fall and a higher AccuM1 in SH Spring. The model simulated PNSDs also agree well with  
500 the measurements in term of the size-dependent standard deviations: relatively smaller standard  
501 deviations for AccuM1 and larger size part of AitkenM and much larger standard deviations for  
502 NuclM, smaller size part of AitkenM, and AccuM2.

503 A detailed comparison indicates the existence of a third PNSD mode peaking around 300–400  
504 nm in the ATom measurements that are not captured by the model. Compared to the observations,  
505 the model-simulated AccuM2 standard deviations are larger in SH Winter and Spring but are  
506 smaller in SH Summer and Fall. In addition, the model overpredicts the number concentration of  
507 particles in the size range of 10–50 nm. These differences may indicate that, in addition to  
508 nucleation, the model may be missing some fundamental microphysical processes of stratospheric  
509 aerosols. Our analysis shows that, in the stratosphere, more particles are charged (positive +  
510 negative) than neutral for particles with diameter larger than  $\sim$ 80 nm and a significant fraction ( $>$   
511 25%) of particles larger than 300 nm carrying multiple charges. We propose that the role of charges  
512 on coagulation and growth of particles in the stratosphere, where ionization rates are high and  
513 particles have very long lifetime, is likely one of such processes. Considering the importance of  
514 accurate particle size distributions (especially the accumulation mode particles) for projecting  
515 realistic radiative forcing response to stratospheric aerosols, it is essential to understand and  
516 incorporate such potentially important processes in model simulations of future changes in the  
517 stratosphere.

518  
519 **Conflict of interest:** The authors declare that they have no conflict of interest.  
520

521 **Acknowledgments.** The MERRA-2 data used in this study have been provided by the Global  
522 Modeling and Assimilation Office (GMAO) at NASA Goddard Space Flight Center. This research  
523 has been supported by NASA (grant nos. 80NSSC19K1275 and 80NSSC21K1199) and  
524 SilverLining.

525 **Data availability.** The GEOS-Chem model is available to the public at <https://geos-chem.seas.harvard.edu/>. Simulation output in this analysis is available at  
526 <https://doi.org/10.5281/zenodo.6909944>. The ATom dataset is published as Wofsy et al., (2021,  
527 <https://doi.org/10.3334/ORNLDAAC/1925>) and is also available at  
528 <https://espoarchive.nasa.gov/archive/browse/atom> (last access: June 2022).  
529



## 530 References

- 531 Brock, C. A., Hamill, P., Wilson, J. C., Jonsson, H. H., and Chan, K. R.: Particle formation in the  
532 upper tropical troposphere – A source of nuclei for the stratospheric aerosol, *Science*, 270,  
533 1650–1653, <https://doi.org/10.1126/science.270.5242.1650>, 1995.
- 534 Brock, C. A., Schröder, F., Kärcher, B., Petzold, A., Busen, R., and Fiebig, M.: Ultrafine particle  
535 size distributions measured in aircraft exhaust plumes, *J. Geophys. Res.-Atmos.*, 105, 26555–  
536 26567, <https://doi.org/10.1029/2000jd900360>, 2000.
- 537 Brock, C. A., Williamson, C., Kupc, A., Froyd, K. D., Erdesz, F., Wagner, N., Richardson, M.,  
538 Schwarz, J. P., Gao, R.-S., Katich, J. M., Campuzano-Jost, P., Nault, B. A., Schroder, J. C.,  
539 Jimenez, J. L., Weinzierl, B., Dollner, M., Bui, T., and Murphy, D. M.: Aerosol size  
540 distributions during the Atmospheric Tomography Mission (ATom): methods, uncertainties,  
541 and data products, *Atmos. Meas. Tech.*, 12, 3081–3099, [https://doi.org/10.5194/amt-12-](https://doi.org/10.5194/amt-12-3081-2019)  
542 3081-2019, 2019.
- 543 Brock, C.A., Froyd, K.D., Dollner, M., Williamson, C.J., Schill, G., Murphy, D.M., Wagner, N.J.,  
544 Kupc, A., Jimenez, J.L., Campuzano-Jost, P., Nault, B.A., Schroder, J.C., Day, D.A., Price,  
545 D.J., Weinzierl, B., Schwarz, J.P., Katich, J.M., Wang, S., Zeng, L., Weber, R., Dibb, J.,  
546 Scheuer, E., Diskin, G.S., DiGangi, J.P., Bui, T., Dean-Day, J.M., Thompson, C.R., Peischl,  
547 J., Ryerson, T.B., Bourgeois, I., Daube, B.C., Commane, R., and Wofsy, S.C. Ambient  
548 aerosol properties in the remote atmosphere from global-scale in situ measurements, *Atmos.*  
549 *Chem. Phys.*, 21: 15023-63. 2021.
- 550 Carn, S. A., Yang, K., Prata, A. J. and Krotkov, N. A.: Extending the long-term record of volcanic  
551 SO<sub>2</sub> emissions with the Ozone Mapping and Profiler Suite nadir mapper. *Geophys. Res. Lett.*,  
552 42: 925– 932. doi: 10.1002/2014GL062437, 2015.
- 553 Dawson, M. L., Varner, M. E., Perraud, V., Ezell, M. J., Gerber, R. B., & Finlayson-Pitts, B. J.:  
554 Simplified mechanism for new particle formation from methanesulfonic acid, amines, and  
555 water via experiments and ab initio calculations. *Proceedings of the National Academy of*  
556 *Sciences*, 109(46), 18719-18724, 2012.
- 557 Dunne, E. M., Gordon, H., Kürten, A., Almeida, J., Duplissy, J., Williamson, C., Ortega, I. K.,  
558 Pringle, K. J., Adamov, A., Baltensperger, U., Barmet, P., Benduhn, F., Bianchi, F.,  
559 Breitenlechner, M., Clarke, A., Curtius, J., Dommen, J., Donahue, N. M., Ehrhart, S., Flagan,  
560 R. C., Franchin, A., Guida, R., Hakala, J., Hansel, A., Heinritzi, M., Jokinen, T., Kangasluoma,  
561 J., Kirkby, J., Kulmala, M., Kupc, A., Lawler, M. J., Lehtipalo, K., Makhmutov, V., Mann,  
562 G., Mathot, S., Merikanto, J., Miettinen, P., Nenes, A., Onnela, A., Rap, A., Reddington, C.  
563 L. S., Riccobono, F., Richards, N. A. D., Rissanen, M. P., Rondo, L., Sarnela, N.,  
564 Schobesberger, S., Sengupta, K., Simon, M., Sipilä, M., Smith, J. N., Stozkhov, Y., Tomé,  
565 A., Tröstl, J., Wagner, P. E., Wimmer, D., Winkler, P. M., Worsnop, D. R., and Carslaw, K.  
566 S.: Global particle formation from CERN CLOUD measurements, *Science*, 354, 1119–1124,  
567 <https://doi.org/10.1126/science.aaf2649>, 2016.
- 568 Eastham, S. D., Weisenstein, D. K., & Barrett, S. R.: Development and evaluation of the unified  
569 tropospheric–stratospheric chemistry extension (UCX) for the global chemistry-transport  
570 model GEOS-Chem. *Atmospheric Environment*, 89, 52-63, 2014.



- 571 English, J. M., Toon, O. B., Mills, M. J., & Yu, F.: Microphysical simulations of new particle  
572 formation in the upper troposphere and lower stratosphere. *Atmospheric Chemistry and*  
573 *Physics*, 11(17), 9303-9322, 2011.
- 574 Evans, M. J., & Jacob, D. J.: Impact of new laboratory studies of N<sub>2</sub>O<sub>5</sub> hydrolysis on global model  
575 budgets of tropospheric nitrogen oxides, ozone, and OH. *Geophysical Research Letters*, 32(9),  
576 2005.
- 577 Gronoff, G., Berkoff, T., Knowland, K. E., Lei, L., Shook, M., Fabbri, B., Carrion, W., & Langford,  
578 A. O.: Case study of stratospheric intrusion above Hampton, Virginia: lidar-observation and  
579 modeling analysis. *Atmospheric Environment*, 118498, 2021.
- 580 Hamill, P., Turco, R. P., Kiang, C. S., Toon, O. B., and Whitten, R. C.: An analysis of various  
581 nucleation mechanisms for sulfate particles in the stratosphere, *J. Aerosol Sci.*, 13, 561–585,  
582 1982.
- 583 Hoesly, R. M., Smith, S. J., Feng, L., Klimont, Z., Janssens-Maenhout, G., Pitkanen, T., Seibert,  
584 J. J., Vu, L., Andres, R. J., Bolt, R. M., Bond, T. C., Dawidowski, L., Kholod, N., Kurokawa,  
585 J.-I., Li, M., Liu, L., Lu, Z., Moura, M. C. P., O'Rourke, P. R., and Zhang, Q.: Historical  
586 (1750-2014) anthropogenic emissions of reactive gases and aerosols from the Community  
587 Emissions Data System (CEDS), *Geosci. Model Dev.*, 11, 369-408, 2018.
- 588 Holmes, C. D., Bertram, T. H., Confer, K. L., Graham, K. A., Ronan, A. C., Wirks, C. K., & Shah,  
589 V.: The role of clouds in the tropospheric NO<sub>x</sub> cycle: A new modeling approach for cloud  
590 chemistry and its global implications. *Geophysical Research Letters*, 46(9), 4980-4990, 2019.
- 591 IPCC. *Climate Change 2021: The Physical Science Basis. Contribution of Working Group I to the*  
592 *Sixth Assessment Report of the Intergovernmental Panel on Climate Change* [Masson-  
593 Delmotte, V., P. Zhai, A. Pirani, S. L. Connors, C. Péan, S. Berger, N. Caud, Y. Chen, L.  
594 Goldfarb, M. I. Gomis, M. Huang, K. Leitzell, E. Lonnoy, J. B. R. Matthews, T. K. Maycock,  
595 T. Waterfield, O. Yelekçi, R. Yu and B. Zhou (eds.)]. Cambridge University Press, 2021.
- 596 Kärcher, B., Turco, R. P., Yu, F., Danilin, M. Y., Weisenstein, D. K., Miake-Lye, R. C., & Busen,  
597 R.: A unified model for ultrafine aircraft particle emissions. *Journal of Geophysical Research:*  
598 *Atmospheres*, 105(D24), 29379-29386, 2000.
- 599 Keller, C. A., Long, M. S., Yantosca, R. M., Da Silva, A. M., Pawson, S., and Jacob D. J.: HEMCO  
600 v1.0: a versatile, ESMF-compliant component for calculating emissions in atmospheric  
601 models, *Geosci. Model Dev.*, 7, 1409–1417, 2014.
- 602 Kerminen, V. M., Chen, X., Vakkari, V., Petäjä, T., Kulmala, M., & Bianchi, F.: Atmospheric new  
603 particle formation and growth: review of field observations. *Environmental Research Letters*,  
604 13(10), 103003, 2018.
- 605 Kirkby, J., Curtius, J., Almeida, J., Dunne, E., Duplissy, J., Ehrhart, S., Franchin, A., Gagné, S.,  
606 Ickes, L., Kürten, A., Kupc, A., Metzger, A., Riccobono, F., Rondo, L., Schobesberger, S.,  
607 Tsagkogeorgas, G., Wimmer, D., Amorim, A., Bianchi, F., Breitenlechner, M., David, A.,  
608 Dommen, J., Downard, A., Ehn, M., Flagan, R. C., Haider, S., Hansel, A., Hauser, D., Jud, W.,  
609 Junninen, H., Kreissl, F., Kvashin, A., Laaksonen, A., Lehtipalo, K., Lima, J., Lovejoy, E. R.,  
610 Makhmutov, V., Mathot, S., Mikkilä, J., Minginette, P., Mogo, S., Nieminen, T., Onnela, A.,  
611 Pereira, P., Petäjä, T., Schnitzhofer, R., Seinfeld, J. H., Sipilä, M., Stozhkov, Y., Stratmann,  
612 F., Tomé, A., Vanhanen, J., Viisanen, Y., Vrtala, A., Wagner, P. E., Walther, H., Weingartner,  
613 E., Wex, H., Winkler, P. M., Carslaw, K. S., Worsnop, D. R., Baltensperger, U., and Kulmala,



- 614 M.: The role of sulfuric acid, ammonia and galactic cosmic rays in atmospheric aerosol  
615 nucleation, *Nature*, 476, 429–433, 2011.
- 616 Kirner, O., Ruhnke, R., Buchholz-Dietsch, J., Jöckel, P., Brühl, C., & Steil, B.: Simulation of polar  
617 stratospheric clouds in the chemistry-climate-model EMAC via the submodel  
618 PSC. *Geoscientific Model Development*, 4(1), 169-182, 2011.
- 619 Knowland, K. E., Keller, C. A., Wales, P. A., Wargan, K., Coy, L., Johnson, M. S., et al. (2022).  
620 NASA GEOS Composition Forecast Modeling System GEOS-CF v1.0: Stratospheric  
621 composition. *Journal of Advances in Modeling Earth Systems*, 14, e2021MS002852.  
622 <https://doi.org/10.1029/2021MS002852>.
- 623 Kravitz, B., Robock, A., Boucher, O., Schmidt, H., Taylor, K. E., Stenchikov, G., & Schulz, M.:  
624 The geoengineering model intercomparison project (GeoMIP). *Atmospheric Science*  
625 *Letters*, 12(2), 162-167, 2011.
- 626 Kulmala, M., Vehkamäki, H., Petäjä, T., Dal Maso, M., Lauri, A., Kerminen, V. M., W. Birmili,  
627 & McMurry, P. H.: Formation and growth rates of ultrafine atmospheric particles: a review  
628 of observations. *Journal of Aerosol Science*, 35(2), 143-176. doi:  
629 10.1016/j.jaerosci.2003.10.003, 2004.
- 630 Kupc, A., Williamson, C., Wagner, N. L., Richardson, M., & Brock, C. A.: Modification,  
631 calibration, and performance of the Ultra-High Sensitivity Aerosol Spectrometer for particle  
632 size distribution and volatility measurements during the Atmospheric Tomography Mission  
633 (ATom) airborne campaign. *Atmospheric Measurement Techniques*, 11(1), 369-383.  
634 doi:10.5194/amt-11-369-2018, 2018.
- 635 Kupc, A., Williamson, C. J., Hodshire, A. L., Kazil, J., Ray, E., Bui, T. P., Dollner, M., Froyd, K.  
636 D., McKain, K., Rollins, A., Schill, G. P., Thames, A., Weinzierl, B. B., Pierce, J. R., and  
637 Brock, C. A.: The potential role of organics in new particle formation and initial growth in  
638 the remote tropical upper troposphere, *Atmos. Chem. Phys.*, 20, 15037-15060, 10.5194/acp-  
639 20-15037-2020, 2020.
- 640 Kürten, A., Bianchi, F., Almeida, J., Kupiainen-Määttä, O., Dunne, E. M., Duplissy, J., Williamson,  
641 C., Barmet, P., Breitenlechner, M., Dommen, J., Donahue, N. M., Flagan, R. C., Franchin,  
642 A., Gordon, H., Hakala, J., Hansel, A., Heinritzi, M., Ickes, L., Jokinen, T., Kangasluoma, J.,  
643 Kim, J., Kirkby, J., Kupc, A., Lehtipalo, K., Leiminger, M., Makhmutov, V., Onnela, A.,  
644 Ortega, I. K., Petäjä, T., Praplan, A. P., Riccobono, F., Rissanen, M. P., Rondo, L.,  
645 Schnitzhofer, R., Schobesberger, S., Smith, J. N., Steiner, G., Stozhkov, Y., Tomé, A., Tröstl,  
646 J., Tsagkogeorgas, G., Wagner, P. E., Wimmer, D., Ye, P., Baltensperger, U., Carslaw, K.,  
647 Kulmala, M., and Curtius, J.: Experimental particle formation rates spanning tropospheric  
648 sulfuric acid and ammonia abundances, ion production rates, and temperatures, *J. Geophys.*  
649 *Res.-Atmos.*, 121, 12377–12400, <https://doi.org/10.1002/2015JD023908>, 2016.
- 650 Laakso, A., Niemeier, U., Visioni, D., Tilmes, S., and Kokkola, H.: Dependency of the impacts of  
651 geoengineering on the stratospheric sulfur injection strategy – Part 1: Intercomparison of  
652 modal and sectional aerosol modules, *Atmos. Chem. Phys.*, 22, 93–118,  
653 <https://doi.org/10.5194/acp-22-93-2022>, 2022.
- 654 Laakso, L., Gagné, S., Petäjä, T., Hirsikko, A., Aalto, P. P., Kulmala, M., & Kerminen, V. M.:  
655 Detecting charging state of ultra-fine particles: instrumental development and ambient  
656 measurements. *Atmospheric Chemistry and Physics*, 7(5), 1333-1345, 2007.





- 657 Lee, S. H., Gordon, H., Yu, H., Lehtipalo, K., Haley, R., Li, Y., & Zhang, R.: New particle  
658 formation in the atmosphere: From molecular clusters to global climate. *Journal of*  
659 *Geophysical Research: Atmospheres*, 124(13), 7098–7146, 2019.
- 660 Lee, S. H., Reeves, J. M., Wilson, J. C., Hunton, D. E., Viggiano, A. A., Miller, T. M., Ballenthin,  
661 J. O., and Lait, L. R.: Particle formation by ion nucleation in the upper troposphere and lower  
662 stratosphere, *Science*, 301, 1886–1889, <https://doi.org/10.1126/science.1087236>, 2003.
- 663 Li, M., Zhang, Q., Kurokawa, J.-I., Woo, J.-H., He, K., Lu, Z., Ohara, T., Song, Y., Streets, D. G.,  
664 Carmichael, G. R., Cheng, Y., Hong, C., Huo, H., Jiang, X., Kang, S., Liu, F., Su, H., and  
665 Zheng, B.: MIX: a mosaic Asian anthropogenic emission inventory under the international  
666 collaboration framework of the MICS-Asia and HTAP, *Atmos. Chem. Phys.*, 17, 935–963,  
667 <https://doi.org/10.5194/acp-17-935-2017>, 2017.
- 668 Lockley, A., MacMartin, D., & Hunt, H.: An update on engineering issues concerning stratospheric  
669 aerosol injection for geoengineering. *Environmental Research Communications*, 2(8),  
670 082001, 2020.
- 671 Lovejoy, E. R., Curtius, J., and Froyd, K. D.: Atmospheric ion-induced nucleation of sulfuric acid  
672 and water, *J. Geophys. Res.*, 109, D08204, <https://doi.org/10.1029/2003JD004460>, 2004.
- 673 Luo, G., Yu, F., & Moch, J. M.: Further improvement of wet process treatments in GEOS-Chem  
674 v12. 6.0: impact on global distributions of aerosols and aerosol precursors. *Geoscientific*  
675 *Model Development*, 13(6), 2879–2903, 2020.
- 676 Martin, R. V., Jacob, D. J., Chance, K., Kurosu, T. P., Palmer, P. I., & Evans, M. J.: Global  
677 inventory of nitrogen oxide emissions constrained by space-based observations of NO<sub>2</sub>  
678 columns. *Journal of Geophysical Research: Atmospheres*, 108(D17), 2003.
- 679 Mills, M. J., Richter, J. H., Tilmes, S., Kravitz, B., MacMartin, D. G., Glanville, A. A., Tribbia, J.  
680 J., Lamarque, J.-F., Vitt, F., Schmidt, A., and Gettelman, A.: Radiative and chemical response  
681 to interactive stratospheric sulfate aerosols in fully coupled CESM1 (WACCM), *J. Geophys.*  
682 *Res.*, 122, 13061–13078, <https://doi.org/10.1002/2017JD027006>, 2017.
- 683 Murphy, D. M., Froyd, K. D., Bourgeois, I., Brock, C. A., Kupc, A., Peischl, J., Schill, G. P.,  
684 Thompson, C. R., Williamson, C. J., and Yu, P.: Radiative and chemical implications of the  
685 size and composition of aerosol particles in the existing or modified global stratosphere,  
686 *Atmos. Chem. Phys.*, 21, 8915–8932, [10.5194/acp-21-8915-2021](https://doi.org/10.5194/acp-21-8915-2021), 2021.
- 687 Murray, L. T., Jacob, D. J., Logan, J. A., Hudman, R. C., & Koshak, W. J.: Optimized regional  
688 and interannual variability of lightning in a global chemical transport model constrained by  
689 LIS/OTD satellite data. *Journal of Geophysical Research: Atmospheres*, 117(D20), 2012.
- 690 Nadykto, A. B., & Yu, F.: Simple correction to the classical theory of homogeneous nucleation.  
691 *The Journal of chemical physics*, 122(10), 104511, 2005.
- 692 NASEM: Reflecting Sunlight: Recommendations for Solar Geoengineering Research and  
693 Research Governance. Washington, DC: The National Academies Press, 2021.
- 694 Pye, H. O., & Seinfeld, J. H.: A global perspective on aerosol from low-volatility organic  
695 compounds. *Atmospheric Chemistry and Physics*, 10(9), 4377–4401, 2010.
- 696 Richter, J., Visioni, D., MacMartin, D., Bailey, D., Rosenbloom, N., Lee, W., Tye, M., and  
697 Lamarque, J.-F.: Assessing Responses and Impacts of Solar climate intervention on the Earth  
698 system with stratospheric aerosol injection (ARISE-SAI), *EGUsphere* [preprint],  
699 <https://doi.org/10.5194/egusphere-2022-125>, 2022.





- 700 Rotman, D. A., Tannahill, J. R., Kinnison, D. E., Connell, P. S., Bergmann, D., Proctor, D., ... &  
701 Kawa, S. R.: Global Modeling Initiative assessment model: Model description, integration,  
702 and testing of the transport shell. *Journal of Geophysical Research: Atmospheres*, 106(D2),  
703 1669-1691, 2001.
- 704 Shepherd, J. G.: *Geoengineering the climate: science, governance and uncertainty*. Royal Society,  
705 2009.
- 706 Shi, Q., Jayne, J. T., Kolb, C. E., Worsnop, D. R., & Davidovits, P.: Kinetic model for reaction of  
707 ClONO<sub>2</sub> with H<sub>2</sub>O and HCl and HOCl with HCl in sulfuric acid solutions. *Journal of*  
708 *Geophysical Research: Atmospheres*, 106(D20), 24259-24274, 2001.
- 709 Stettler, M.E.J., S. Eastham, S.R.H. Barrett (2011), Air quality and public health impacts of UK  
710 airports. Part I: Emissions, *Atmos. Environ.*, 45, 5415-5424, 2011.
- 711 Svensmark, J., Shaviv, N. J., Enghoff, M. B., & Svensmark, H.: The ION-CAGE code: A  
712 numerical model for the growth of charged and neutral aerosols. *Earth and Space Science*. 7,  
713 e2020EA001142. <https://doi.org/10.1029/2020EA001142>, 2020.
- 714 Thompson, C.R., Wofsy, S.C., Prather, M.J., Newman, P.A., Hanisco, T.F., Ryerson, T.B., Fahey,  
715 D.W., Apel, E.C., Brock, C.A., Brune, W.H., Froyd, K., Katich, J.M., Nicely, J.M., Peischl,  
716 J., Ray, E., Veres, P.R., Wang, S., Allen, H.M., Asher, E., Bian, H., Blake, D., Bourgeois, I.,  
717 Budney, J., Bui, T.P., Butler, A., Campuzano-Jost, P., Chang, C., Chin, M., Commane, R.,  
718 Correa, G., Crouse, J.D., Daube, B., Dibb, J.E., DiGangi, J.P., Diskin, G.S., Dollner, M.,  
719 Elkins, J.W., Fiore, A.M., Flynn, C.M., Guo, H., Hall, S.R., Hannun, R.A., Hills, A., Hints,  
720 E.J., Hodzic, A., Hornbrook, R.S., Huey, L.G., Jimenez, J.L., Keeling, R.F., Kim, M.J., Kupe,  
721 A., Lacey, F., Lait, L.R., Lamarque, J.-F., Liu, J., McKain, K., Meinardi, S., Miller, D.O.,  
722 Montzka, S.A., Moore, F.L., Morgan, E.J., Murphy, D.M., Murray, L.T., Nault, B.A.,  
723 Neuman, J.A., Nguyen, L., Gonzalez, Y., Rollins, A., Rosenlof, K., Sargent, M., Schill, G.,  
724 Schwarz, J.P., Clair, J.M.S., Steenrod, S.D., Stephens, B.B., Strahan, S.E., Strode, S.A.,  
725 Sweeney, C., Thames, A.B., Ullmann, K., Wagner, N., Weber, R., Weinzierl, B., Wennberg,  
726 P.O., Williamson, C.J., Wolfe, G.M., and Zeng, L. 'The NASA Atmospheric Tomography  
727 (ATom) Mission: Imaging the Chemistry of the Global Atmosphere', *Bulletin of the*  
728 *American Meteorological Society*, 103: E761-E90. 2022.
- 729 Turco, R. P., Whitten, R. C., & Toon, O. B.: Stratospheric aerosols: Observation and theory.  
730 *Reviews of Geophysics*, 20(2), 233-279. doi: 10.1029/RG020i002p00233, 1982.
- 731 van der Werf, G. R., J. T. Randerson, L. Giglio, T. T. van Leeuwen, Y. Chen, B. M. Rogers, M.  
732 Mu, M. J. E. van Marle, D. C. Morton, G. J. Collatz, R. J. Yokelson, and P. S. Kasibhatla,  
733 *Global fire emissions estimates during 1997–2016*, *Earth Sys. Sci. Data*, 9, 697-720, 2017.
- 734 van Donkelaar, A., Martin, R.V., Leaitch, W.R., Macdonald, A.M., Walker, T.W., Streets, D.G.,  
735 Zhang, Q., Dunlea, E.J., Jimenez, J.L., Dibb, J.E., Huey, L.G., Weber, R., Andreae, M.O.:  
736 Analysis of aircraft and satellite measurements from the Intercontinental Chemical Transport  
737 Experiment (INTEX-B) to quantify long-range transport of East Asian sulfur to  
738 Canada. *Atmospheric Chemistry and Physics*, 8(11), 2999-3014, 2008.
- 739 Vehkamäki, H., Kulmala, M., Napari, I., Lehtinen, K. E., Timmreck, C., Noppel, M., & Laaksonen,  
740 A.: An improved parameterization for sulfuric acid–water nucleation rates for tropospheric  
741 and stratospheric conditions. *Journal of Geophysical Research: Atmospheres*, 107(D22),  
742 AAC-3. doi: 10.1029/2002JD002184, 2002.



- 743 Weisenstein, D. K., Visionsi, D., Franke, H., Niemeier, U., Vattioni, S., Chiodo, G., Peter, T., and  
744 Keith, D. W.: An interactive stratospheric aerosol model intercomparison of solar  
745 geoengineering by stratospheric injection of SO<sub>2</sub> or accumulation-mode sulfuric acid  
746 aerosols, *Atmos. Chem. Phys.*, 22, 2955–2973, <https://doi.org/10.5194/acp-22-2955-2022>,  
747 2022.
- 748 Williamson, C., Kupc, A., Wilson, J., Gesler, D. W., Reeves, J. M., Erdesz, F., McLaughlin, R., &  
749 Brock, C. A.: Fast time response measurements of particle size distributions in the 3–60 nm  
750 size range with the nucleation mode aerosol size spectrometer. *Atmospheric Measurement*  
751 *Techniques*, 11(6), 3491–3509. doi:10.5194/amt-11-3491-2018, 2018.
- 752 Williamson, C. J., Kupc, A., Axisa, D., Bilsback, K. R., Bui, T., Campuzano-Jost, P., Dollner, M.,  
753 Froyd, K. D., Hodshire, A. L., Jimenez, J. L., Kodros, J. K., Luo, G., Murphy, D. M., Nault,  
754 B. A., Ray, E. A., Weinzierl, B., Wilson, J. C., Yu, F. Q., Yu, P. F., Pierce, J. R., and Brock,  
755 C. A.: A large source of cloud condensation nuclei from new particle formation in the tropics,  
756 *Nature*, 574, 399–403, <https://doi.org/10.1038/s41586-019-1638-9>, 2019.
- 757 Williamson, C. J., Kupc, A., Rollins, A., Kazil, J., Froyd, K. D., Ray, E. A., Murphy, D. M., Schill,  
758 G. P., Peischl, J., Thompson, C., Bourgeois, I., Ryerson, T. B., Diskin, G. S., DiGangi, J. P.,  
759 Blake, D. R., Bui, T. P. V., Dollner, M., Weinzierl, B., and Brock, C. A.: Large hemispheric  
760 difference in nucleation mode aerosol concentrations in the lowermost stratosphere at mid-  
761 and high latitudes, *Atmos. Chem. Phys.*, 21, 9065–9088, [https://doi.org/10.5194/acp-21-](https://doi.org/10.5194/acp-21-9065-2021)  
762 [9065-2021](https://doi.org/10.5194/acp-21-9065-2021), 2021.
- 763 Wofsy, S.C., S. Afshar, H.M. Allen, E.C. Apel, E.C. Asher, B. Barletta, J. Bent, H. Bian, B.C.  
764 Biggs, D.R. Blake, N. Blake, I. Bourgeois, C.A. Brock, W.H. Brune, J.W. Budney, T.P. Bui,  
765 A. Butler, P. Campuzano-Jost, C.S. Chang, M. Chin, R. Commane, G. Correa, J.D. Crounse,  
766 P. D. Cullis, B.C. Daube, D.A. Day, J.M. Dean-Day, J.E. Dibb, J.P. DiGangi, G.S. Diskin,  
767 M. Dollner, J.W. Elkins, F. Erdesz, A.M. Fiore, C.M. Flynn, K.D. Froyd, D.W. Gesler, S.R.  
768 Hall, T.F. Hanisco, R.A. Hannun, A.J. Hills, E.J. Hints, A. Hoffman, R.S. Hornbrook, L.G.  
769 Huey, S. Hughes, J.L. Jimenez, B.J. Johnson, J.M. Katich, R.F. Keeling, M.J. Kim, A. Kupc,  
770 L.R. Lait, K. McKain, R.J. McLaughlin, S. Meinardi, D.O. Miller, S.A. Montzka, F.L. Moore,  
771 E.J. Morgan, D.M. Murphy, L.T. Murray, B.A. Nault, J.A. Neuman, P.A. Newman, J.M.  
772 Nicely, X. Pan, W. Paplawsky, J. Peischl, M.J. Prather, D.J. Price, E.A. Ray, J.M. Reeves, M.  
773 Richardson, A.W. Rollins, K.H. Rosenlof, T.B. Ryerson, E. Scheuer, G.P. Schill, J.C.  
774 Schroder, J.P. Schwarz, J.M. St.Clair, S.D. Steenrod, B.B. Stephens, S.A. Strode, C. Sweeney,  
775 D. Tanner, A.P. Teng, A.B. Thames, C.R. Thompson, K. Ullmann, P.R. Veres, N.L. Wagner,  
776 A. Watt, R. Weber, B.B. Weinzierl, P.O. Wennberg, C.J. Williamson, J.C. Wilson, G.M.  
777 Wolfe, C.T. Woods, L.H. Zeng, and N. Vieznor. 2021. ATom: Merged Atmospheric  
778 Chemistry, Trace Gases, and Aerosols, Version 2. ORNL DAAC, Oak Ridge, Tennessee,  
779 USA. <https://doi.org/10.3334/ORNLDAAC/1925>.
- 780 Yu, F., & Luo, G.: Simulation of particle size distribution with a global aerosol model: contribution  
781 of nucleation to aerosol and CCN number concentrations. *Atmospheric Chemistry and*  
782 *Physics*, 9(20), 7691–7710, 2009.
- 783 Yu, F., & Turco, R. P.: Ultrafine aerosol formation via ion-mediated nucleation. *Geophysical*  
784 *Research Letters*, 27(6), 883–886. doi: 10.1029/1999GL011151, 2000.



- 785 Yu, F., Nadykto, A. B., Herb, J., Luo, G., Nazarenko, K. M., & Uvarova, L. A.: H<sub>2</sub>SO<sub>4</sub>-H<sub>2</sub>O-NH<sub>3</sub>  
786 ternary ion-mediated nucleation (TIMN): kinetic-based model and comparison with CLOUD  
787 measurements. *Atmospheric Chemistry and Physics*, 18(23), 17451-17474, 2018.
- 788 Yu, F., Nadykto, A. B., Luo, G., & Herb, J.: H<sub>2</sub>SO<sub>4</sub>-H<sub>2</sub>O binary and H<sub>2</sub>SO<sub>4</sub>-H<sub>2</sub>O-NH<sub>3</sub> ternary  
789 homogeneous and ion-mediated nucleation: lookup tables version 1.0 for 3-D modeling  
790 application. *Geoscientific Model Development*, 13(6), 2663-2670, 2020.
- 791 Zhang, R., Khalizov, A., Wang, L., Hu, M., & Xu, W.: Nucleation and growth of nanoparticles in  
792 the atmosphere. *Chemical reviews*, 112(3), 1957-2011, 2012.
- 793